



# Reduction and oxidation kinetics of Co–Ni/Al<sub>2</sub>O<sub>3</sub> oxygen carrier involved in a chemical-looping combustion cycles

Mohammad M. Hossain, Hugo I. de Lasa\*

Chemical Reactor Engineering Center and Department of Chemical & Biochemical Engineering, The University of Western Ontario, London, ON, Canada

## ARTICLE INFO

### Article history:

Received 1 July 2008

Received in revised form 2 January 2009

Accepted 29 January 2009

Available online 10 February 2009

### Keywords:

CO<sub>2</sub> capture

CLC

Gas–solid reaction kinetics

Nucleation and nuclei growth model

Shrinking-core model

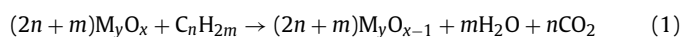
## ABSTRACT

The solid-state kinetics of Co–Ni/Al<sub>2</sub>O<sub>3</sub> oxygen carrier is studied using non-isothermal reaction data and a non-linear regression analysis. XRD analysis of the fresh samples shows that NiO is the dominant reducible phase of the oxygen carrier. Pulse chemisorption suggests a negligible nuclei growth over the repeated reduction/oxidation cycles. Mercury porosimetry confirms that the pore size of the carrier particle is slightly increased following reduction. A nucleation and nuclei growth model and an unreacted shrinking-core model are developed based on the oxygen carrier texture change during reduction/oxidation, as observed by pulse chemisorption and mercury porosimetry. Model parameters are calculated using H<sub>2</sub>-TPR and O<sub>2</sub>-TPO data. It is found that the random nucleation model describes solid phase changes adequately. The determined apparent activation energies are 45 and 44 kJ/mol for the reduction and oxidation, respectively. The established kinetic model is successfully evaluated for the reduction cycle using a CREC mini-fluidized Riser Simulator reactor operating under expected conditions of large industrial scale fluidized CLC units.

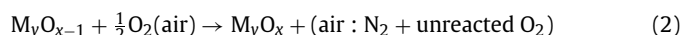
© 2009 Published by Elsevier Ltd.

## 1. Introduction

It is generally accepted that the emission of CO<sub>2</sub> gas is primarily responsible for global warming, which leads the world community to investigate alternative technologies in order to reduce CO<sub>2</sub> drastically. The available CO<sub>2</sub> capture technologies are energy intensive and costly. As a result, important research is currently being developed to improve efficiencies and to reduce CO<sub>2</sub> sequestration cost. In this regard, chemical-looping combustion (CLC) is possibly the most promising CO<sub>2</sub> sequestration technologies. CLC is configured with two interconnected fluidized bed reactors: an air reactor and a fuel reactor (Fig. 1). A solid oxygen carrier is circulated between the reactors to transfer oxygen from air to fuel reactor. In CLC, the fuel is fed into the fuel reactor where it is oxidized by the lattice oxygen of the metal oxide. Complete combustion in the fuel reactor produces CO<sub>2</sub> and water vapor. Therefore, the CO<sub>2</sub> formed can be readily recovered by condensing water vapor, eliminating the need of an additional energy intensive CO<sub>2</sub> separation. The free-of-water CO<sub>2</sub> can be sequestered or/and used for other applications. A generalized description of the overall reaction stoichiometry in the fuel reactor can be written as follows:



Once fuel oxidation completed the reduced metal oxide M<sub>y</sub>O<sub>x-1</sub> (or metal) is transported to the air reactor where it is re-oxidized according to the following reaction:



The outlet gas stream of the air reactor contains nitrogen and unreacted oxygen. These gases can be released to the atmosphere with minimum negative environmental impact.

Thus, the main advantage of CLC is the inherent separation of both CO<sub>2</sub> and H<sub>2</sub>O from the flue gases. In addition, CLC also minimizes NO<sub>x</sub> formation since the fuel burns in the fuel reactor in an air free environment and the reduced oxygen carrier is re-oxidized in the air reactor in the absence of a fuel, at comparatively lower temperatures. NO<sub>x</sub> formation usually occurs well above 1200 °C a potentially maximum temperature for CLC (Ishida and Jin, 1996).

Transition metal oxides such as NiO, CuO, CoO, Fe<sub>2</sub>O<sub>3</sub> and Mn<sub>2</sub>O<sub>3</sub> are considered as possible candidates for oxygen carrier (Hossain and de Lasa, 2008; Adanez et al., 2004). A suitable metal oxide is deposited on an inert material such as SiO<sub>2</sub>, TiO<sub>2</sub>, ZrO<sub>2</sub>, Al<sub>2</sub>O<sub>3</sub> and YSZ (yttria-stabilized zirconia), in order to achieve fluidizable characteristics of the carrier materials.

Regarding the reaction kinetics and in spite of being very critical in determining the process design and performance, only a very limited number of contributions consider the solid-state kinetics of the reduction/oxidation reactions involved in CLC. Even more and until very recently there was not a single contribution, we are aware of, addressing phenomenological based reaction kinetics. The published

\* Corresponding author.

E-mail address: [hdelasa@eng.uwo.ca](mailto:hdelasa@eng.uwo.ca) (H.I. de Lasa).

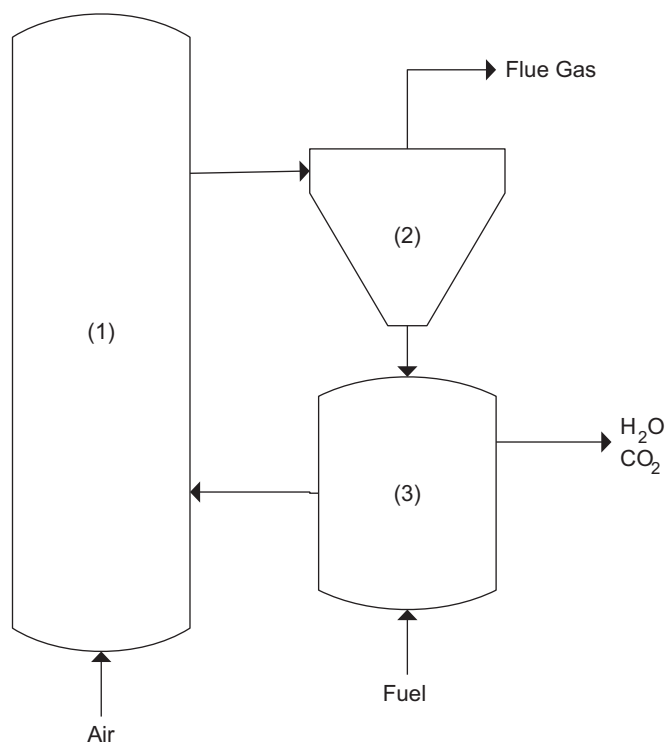


Fig. 1. Schematic view of chemical-looping combustion: (1) regenerator reactor, (2) cyclone and (3) fuel reactor.

papers only evaluated either a power law or an unreacted shrinking-core model to describe the data for reduction/oxidation cycles (Ishida and Jin, 1996; Jin et al., 1999; Ryu et al., 2001; Garcia-Labiano et al., 2006; Abad et al., 2007).

One can notice however, that there are literature references considering reduction/oxidation of bulk metals for methane reforming catalysts. In this area two types of kinetic models have been considered: (1) nucleation and nuclei growth model (Koga and Harrison, 1984; Richardson et al., 1996, 2004) and (2) unreacted shrinking-core model (Richardson et al., 2004; Utigard et al., 2005; Sohn and Szekely, 1972; Szekely et al., 1973). According to the nucleation and nuclei growth model, the gas–solid reaction proceeds as: (a) activation of sites, (b) formation of nuclei, (c) growth and further formation of nuclei, (d) overlap of nuclei, (e) ingestion of a nucleation site and (f) continue crystal growth (Brown, 2001). The nucleation model only emphasizes on the chemical mechanism and kinetics of the gas–solid reactions, but it does not consider the morphological factors, which may equally be important as topological properties in determining the adequate kinetics. For instance, gas–solid reaction rate could be influenced by the grain size above a particle diameter  $10\ \mu\text{m}$  (Richardson et al., 2003). Very specially and for the porous particles the particle size and its status during the course of reaction is very important in determining the reaction rates. For instance, the shrinking-core model enables to account for the dependence of the particle size and pore structure of solid reactant particles. This model considers that the metal–metal oxide interface moves towards the center of the grain, leaving behind a porous metallic/metal oxide product layer through which the gaseous reactant and product diffuses (Szekely et al., 1973; Levenspiel, 1999). Depending on temperature, solid particle size and porosity the overall reaction can be either chemical reaction controlled or internal diffusion controlled. For the chemical reaction controlled case, the reaction proceeds uniformly throughout the solid particles, with each grain undergoing the same shrinking-core kinetics. For the diffusion controlled re-

actions, a sharp reaction front or interface exists in the particle that moves progressively towards the particle center (Richardson et al., 2003; Szekely et al., 1973).

Gas–solid reaction kinetics becomes more complicated for supported metal/metal oxides materials, given the potentially limited accessibility to the metal/metal oxide, which may depend on both metal and support properties. Thus, even if the physical properties of the particle such as shape, size together with pore size distribution may have an influence, in many cases there may be a dominant support contribution affecting metal–support interaction and the orientation of the active components. In the case of a bulk metal oxide, upon reduction, the metal atoms released from the oxide rapidly agglomerate and sinter forming large metal crystallites. For supported metal oxides system however, the metal oxide grains are isolated. Therefore, after reduction the metal atoms must either coalesce with the grain to form small crystallites or migrate over the support to nucleation sites, where the crystallite growth occurs (Richardson et al., 2004). The following are the possible mechanistic steps for the reduction of Ni/Al<sub>2</sub>O<sub>3</sub> material using hydrogen as reducing gas: (a) dissociation of hydrogen first on the NiO and then on the surface of Ni<sup>0</sup> clusters as soon they became available, (b) breaking of Ni–O bonds, to produce more Ni<sup>0</sup> atoms and H<sub>2</sub>O molecules. This step can be accelerated or decelerated by foreign cations in the NiO lattice or on the surface, (c) diffusion of nickel atoms across the support surface away from the center of the reduction, (d) nucleation of nickel atoms into metallic clusters, after a possible induction period and (e) crystal growth (Richardson et al., 2004; Gavalas et al., 1984).

The present study reports the solid-state reaction mechanism and kinetics of the reduction and oxidation of Co–Ni/Al<sub>2</sub>O<sub>3</sub> oxygen carrier involved in CLC. The phenomenological kinetics models considered are established based on the physical and chemical characterization results of the oxygen carrier studied. The rate-controlling step of the gas–solid reactions in CLC process is defined by observing the reaction rates at different set of experimental conditions as well as applying theoretical calculations. Kinetics parameters are assessed using temperature programmed reduction (TPR) and temperature programmed (oxidation TPO) data and validated employing reaction data obtained in a CREC Riser Simulator reactor.

## 2. Experimental

### 2.1. Preparation of the oxygen carrier

The bimetallic Co–Ni/ $\alpha$ -Al<sub>2</sub>O<sub>3</sub> oxygen carriers were prepared according to the incipient wetness technique. The  $\alpha$ -alumina (65% Al<sub>2</sub>O<sub>3</sub>, 34.8% H<sub>2</sub>O and 0.15% Na<sub>2</sub>O) used as support in oxygen carrier preparation was provided by Stream Chemicals Inc., USA. Prior to metal loading the  $\alpha$ -alumina was calcined at 1000 °C for 8 hours. Three steps were involved in oxygen carrier preparation: support impregnation, reduction, and calcination. The details of the preparation method can be found elsewhere (Hossain et al., 2007; Hossain and de Lasa, 2007; Sedor et al., 2008a,b).

### 2.2. Pulse chemisorptions, X-ray diffraction (XRD) and porosity

Pulse chemisorption experiments were conducted to determine active surface area, percent metal dispersion and active particle size using a Micromeritics AutoChem II 2920 analyzer. To perform a pulse chemisorption experiment, a stream of argon gas flowed through a bed of pre-reduced carrier at a rate of 50 mL/min. A series of hydrogen pulses (1.0 mL) were injected into the system at ambient temperature. A TCD detector analyzed the exit gas from the sample. As hydrogen gas was adsorbed by the sample, peaks were created in the TCD reading of the outlet stream. A pulse chemisorption experiment was completed when two consecutive peaks had the same area.

The morphology of the prepared oxygen carrier materials was studied using XRD. The XRD experiments were performed in a Rigaku spectrometer at ambient temperature using Cu-K $\alpha$  radiation ( $\lambda = 1.542 \text{ \AA}$ ) at 10 kV and 50 mA. The scan speed was 2 scan/min and  $2\theta$  value was ranging from  $5^\circ$  to  $60^\circ$ . The crystallite sizes of NiO and Ni were calculated using Scherrer equation (Lemaitre et al., 1984).

$$d_{\text{XRD}} = \frac{0.9\lambda}{(\beta - \beta_0) \cos \theta} \quad (3)$$

where,  $d_{\text{XRD}}$  is the volume average diameter of the crystallite,  $(\beta - \beta_0)$  is the full width at half maxima of the peak.

The porosity of the solid samples was measured in a Micromeritics Mercury Pore Sizer 9010. This instrument determines the pore size of solid particles by assuming a cylindrical pore using the following equation:

$$d_{\text{pore}} = -\frac{4\sigma \cos \theta}{P_a} \quad (4)$$

where,  $P_a$  applied pressure,  $\sigma$  is the surface tension and  $\theta$  is the contact angle.

### 2.3. Temperature programmed reduction/oxidation

The reduction/oxidation kinetics was determined using the temperature programmed reaction data. Both the TPR and TPO experiments were conducted using a Micromeritics AutoChem II 2920 analyzer. A 100–200 mg of oxygen carrier sample was loaded in a U-shaped quartz reactor tube and this tube was placed into the sample port, located inside a heating element. The details of the TPR/TPO experimental methods for kinetic analysis can be found in Hossain and de Lasa (2007).

### 2.4. Kinetics experiments in the CREC riser simulator

Apart from the TPR experiments, the kinetics of the oxygen carrier reduction was also established using the CREC Riser Simulator data under expected conditions of an industrial scale fluidized CLC unit. The CREC Riser Simulator is a bench scale mini-fluidized bed reactor, invented at CREC-UWO (de Lasa, 1992). A schematic diagram of the CREC Riser Simulator set-up and details of the experimental procedure can be found elsewhere (Hossain, 2007; Hossain and de Lasa, 2007; Hossain et al., 2007).

## 3. Results and discussions

### 3.1. Physicochemical characterization of the oxygen carrier

Fluidizability is an important characteristic that an oxygen carrier should have for its application in CLC. Therefore, it is important to analyze the particles size and size distribution of the prepared oxygen carrier to confirm its adequacy for fluidized bed conditions. Beside the fluidization properties, the size of particles also plays a significant role in gas–solid reactions involved in fuel and air reactors. For instance, large particles limit the gas phase reactant access to the oxides inner layers of the oxygen carrier. As a result, using smaller particles, the diffusional resistance can be minimized and reduction/oxidation rates can be maximized. On the other hand, excessive smaller particles can cause fluidization problems, channeling and loss of fines.

Considering the importance of the above mentioned facts, the particle size of the prepared oxygen carrier was determined by using a Malvern Mastersizer 2000 size analyzer. Fig. 2 shows the particle size distribution of a Co–Ni/Al<sub>2</sub>O<sub>3</sub> oxygen carrier sample with a size range between 10 and 110  $\mu\text{m}$ . Once the particle size distribution

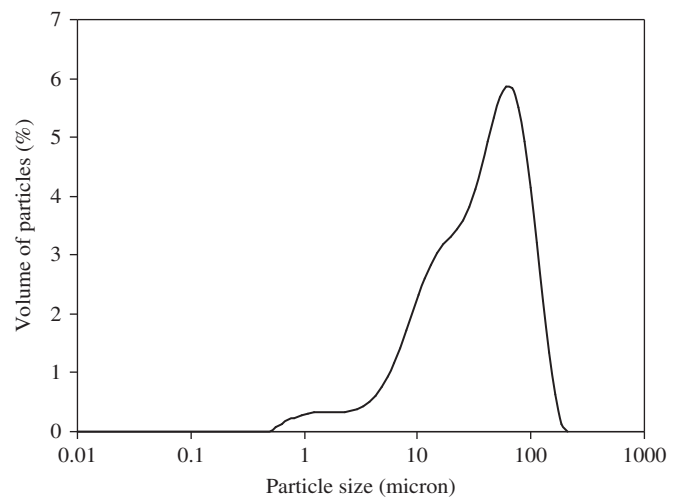


Fig. 2. Particle size distribution of a Co–Ni/Al<sub>2</sub>O<sub>3</sub> oxygen carrier sample.

was determined, the surface-volume mean (Sauter mean) diameter was calculated using the particle size distribution and the following formula:

$$d_{\text{psm}} = \frac{1}{\sum_{i=1}^n \frac{x_i}{d_{pi}}} \quad (5)$$

where, the calculated Sauter mean diameter was found to be 95  $\mu\text{m}$ .

Considering the 1500 kg/m<sup>3</sup> particle density ( $\rho_p$ ) and the average particle size measured, it was shown that the prepared oxygen carrier falls in Group A of Geldart's powder classification. One should notice that the widely used fluid catalytic cracking (FCC) catalysts also belong to this type of powders. Based on this comparison, it can be concluded that the oxygen carrier prepared in this study should fluidize well. These characteristics were further confirmed experimentally using a plexiglas model of the CREC Riser Simulator, specially manufactured for flow visualization.

In a fluidized bed CLC process when the supported metal oxide carrier material undergoes repeated reduction/oxidation cycles the following complications might arise: (1) metal support interaction (2) preferred orientation of the active component (3) changed morphology and accessibility of the active species and (4) altered particle shape, size and pore size distribution (Richardson et al., 1994). The physicochemical characterization of the supported oxygen carrier materials provides complete insight into the complex phenomenon and mechanisms. It also helps understanding the possible structural change of the particles during the repeated redox cycles.

XRD studies were carried out to identify the different phases of the nickel species present in the supported oxygen carrier. Fig. 3 shows the X-ray patterns of a calcined oxygen carrier after exposing to multiple CLC cycles samples. In the X-ray, a strong signal for NiO at  $2\theta = 43.519^\circ$  and relatively smaller peak for NiCo<sub>2</sub>O<sub>4</sub> species at  $2\theta = 37.519^\circ$  was observed. No Co<sub>3</sub>O<sub>4</sub> peak was observed in the XRD patterns, which is understandably due to the low concentration of Co (0.5%) in the carrier material. However, this small amount of Co shows significant effect in influencing the alumina support to minimize the NiAl<sub>2</sub>O<sub>4</sub> formation (Hossain et al., 2007; Hossain and de Lasa, 2007). Generally, nickel has tendency to react with alumina to form nickel aluminate, which is difficult to reduce under CLC reaction conditions. Co having important affinity to interact with Al<sub>2</sub>O<sub>3</sub> forms cobalt aluminate. Thus replacing a relatively small fraction of Ni by an equivalent amount of Co appears to help minimizing the undesirable formation of aluminate (Bolt et al., 1998).

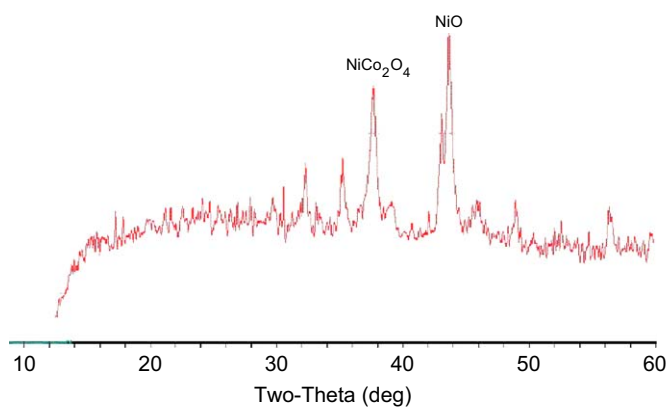


Fig. 3. X-ray diffractogram of a freshly calcined Co-Ni/Al<sub>2</sub>O<sub>3</sub> sample.

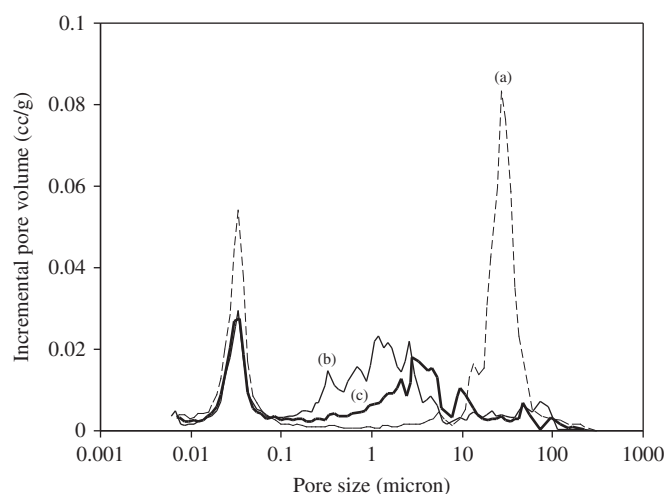


Fig. 4. Pore size distribution of oxygen carriers using Hg porosimetry: (a)  $\alpha$ -Al<sub>2</sub>O<sub>3</sub>, (b) calcined Co-Ni/Al<sub>2</sub>O<sub>3</sub> and (c) reduced Co-Ni/Al<sub>2</sub>O<sub>3</sub> sample.

Considering a crystallite spherical shape, the average crystallite size NiO/Ni can be determined from Scherrer equation (Eq. (3)) using the width of the half maximum of the most intense peak of NiO/Ni of the XRD patterned. A narrow NiO peak suggests large crystal size, while a broad peak corresponds to small crystal size. On this basis, it was observed that the particle size of NiO was about 34.4 nm and it remained unchanged after exposing the sample into multiple reduction/oxidation cycles in CLC processes. The size of Ni crystal (reduced sample) was shown to be smaller (28.1 nm) than that of nickel oxide, which is consistent with the fact that the molar volume of Ni is smaller than that of NiO. The crystal size of the reduced sample was also estimated from H<sub>2</sub> chemisorption, which suggests the size of the crystal approximately 85 nm. From chemisorptions results, it is also apparent that the metal crystal size of the sample remained almost constant over repeated redox cycles, which is an indication of the absence of metal sintering. Relatively high and stable metallic surface area of the Co promoted carrier further supports the uniform and unchanged metal particle size (Hardiman et al., 2004, 2005; Takanabe et al., 2005).

Regarding the pore size distribution, it was found that it is of the bimodal type for the bare alumina support (Fig. 4). The first peak represents the pore sizes between 10  $\mu$ m and 100  $\mu$ m while the second peak consists of the pore size from 0.01  $\mu$ m to 0.1  $\mu$ m. Impregnation of the alumina with Ni/Co nitrate provides a pore size distribution close to the one for bare alumina, with the first peak

shifting towards the lower range of pores (Fig. 4). This decreased porosity is attributed to the partial clogging of the large support pores by metal species, making them less accessible for mercury intrusion. One should also notice that the second peak remaining essentially unchanged after metal loading, suggests that the metal/metal oxide particles are larger than the largest pore in this pore size distribution. This observation is consistent with the crystallite size (approximately 85 nm) estimated by H<sub>2</sub> chemisorption, with this size being smaller than the larger pores (first peak and) and larger than the pores of the second peak. Therefore, one can conclude that the crystallite sizes estimated by pulse chemisorption seem more reliable than those estimated from Scherrer equation using XRD peaks. One can also notice that after reduction the porosity of the carrier material is slightly increased possibly due to the shrinkage of the crystal volume (NiO  $\rightarrow$  Ni) inside the pores. A similar relation between the support pore size distribution and the metal particle size were reported by Khodakov et al. (2002, 2003) in case of a silica supported Co catalysts.

### 3.2. Kinetics modeling

#### 3.2.1. The phenomena involved

The CLC process involves gas–solid reactions. Before reacting with the solid reactant, the gas molecules must be transported to the reaction site by: (i) transfer from the bulk gas phase to the surface of the solid oxygen carrier and (ii) diffusion through the porous structure and through the blanket of the ash to the surface of the unreacted core. Following the transport steps, it involves: (iii) adsorption of the gas molecule on the active sites and (iv) reaction between adsorbed molecules and the solid phase. Finally, the gaseous product desorbs and transport to the bulk gas phase through steps (i) and (ii) but in the opposite direction. The above steps have their own kinetics that can limit or influence the overall rate of the reaction. The resistances of the different steps also vary significantly. In such situations only the highest resistance must be considered as rate-limiting step.

The rate-controlling steps of the gas–solid reactions involve in CLC process can be deduced by observing the reaction rate at different set of reaction conditions. The global reaction is considered to be the intrinsic if there are no transport limitations. Therefore, the first matter to examine is the possibility of transport limitations and the potential like hood to eliminate them. Otherwise this step has to be accounted for. The external mass transfer limitation mainly depends on the particle size, the velocity between solid particle and fluid and the fluid properties. In the context of the present study, the external and internal transport limitations were assessed with Froessling's dimensionless correlations and Weisz-Prater criterion, respectively using the experimental data (Fogler, 1999; Heynderickx et al., 2005). Under the studied reaction conditions, the kinetics of both the reduction and oxidation cycles has been found to be free from transport limitations (detail analysis can be found in Hossain and de Lasa, 2007).

#### 3.2.2. Phenomenological kinetics models

The intrinsic kinetics of the gas–solid reaction in a CLC process can be formulated considering an overall reaction rate being a function of the degree of reduction/oxidation of solid material  $f(\alpha)$  and the composition of the species in the gas-phase (Kanervo and Krause, 2001, 2002):

$$\frac{d\alpha}{dt} = k(T)f(\alpha)f(p_A, p_B) \quad (6)$$

where,  $\alpha$  is the progress of the reaction, which can be expressed in different ways based on the available measured variable(s). Usually, the extent of reaction is defined in terms of the change of mass of the sample or an equivalent basis in terms of gas/heat consumed or evolved.

The degree of reduction and oxidation of the supported oxygen carriers is defined using the hydrogen and oxygen consumption data, for the respective reactions. Based on the TPR/TPO profile analysis, the transient solid conversion ( $\alpha$ ) during each solid-state reaction can be obtained from

$$\alpha = \frac{\Delta n_t}{\Delta n_{total}} \quad (7)$$

where,  $\Delta n_t$  represents the moles of hydrogen or moles of oxygen consumed at time  $t$  (min) and  $\Delta n_{total}$  the total moles of hydrogen or moles of oxygen consumed for the complete reduction or oxidation of the oxygen carrier sample.

The function  $f(p_A, p_B)$  of Eq. (6) can be lumped in a single pseudo-constant given all the TPR/TPO were carried out at same feed flow rate, hydrogen/oxygen partial pressure, essentially free of water and differential conversion. Under these assumptions Eq. (6) can be reduced to

$$\frac{d\alpha}{dt} = k(T)f(\alpha) \quad (8)$$

with the rate constant ( $k$ ) given by the Arrhenius equation

$$k = k_0 \exp \left[ \frac{-E_{app}}{R} \left( \frac{1}{T} - \frac{1}{T_m} \right) \right] \quad (9)$$

where,  $E_{app}$  is the activation energy and  $k_0$  the pre-exponential factor and  $T_m$  being the centering temperature to minimize cross-correlation between parameters. The function of the degree of conversion ( $f(\alpha)$ ) depends on the model applied in the determination of the kinetics.

**3.2.2.1. Nucleation and nuclei growth model.** According to this model the gas–solid reactions proceeds by nucleation (nuclei formation) and subsequent nuclei growth. Before nucleation there is an induction period in order to activate the solid phase to form nuclei. The length of the induction period primarily depends on the gas–solid system and reaction temperature. Nucleation is a dynamic process, which practically initiates the reaction. The progress of the reaction then continues with nucleation and growth of the already formed nuclei. The nuclei growth occurs due to the overlap of the nuclei and/or ingestion of a nuclei site. The overall conversion of the reaction is determined by the relative rate of nucleation, nuclei growth and the concentration of the potential nucleus-forming sites (also called germ nuclei). For a particular gas–solid reaction the nuclei growth rate is constant at a given temperature and composition of the gas phase. Fig. 5 shows the possible steps during a gas–solid reaction following the nucleation and nuclei growth model.

As it can be seen, following an induction period, both reduction and oxidation involve multiple steps, such as formation of nuclei, crystal growth, dislocation and point defects. Either for nucleation and nuclei growth or their combination the rate-determining step of the overall reaction and the energetics of the reaction process is primarily dependent upon the rate-determining step. Generally, the experimental  $\alpha$ – $t$  (conversion–time) profiles of a gas–solid reaction shows a sigmoid shape (Richardson et al., 2004; Hossain and de Lasa, 2007; Sedor et al., 2008a,b). This type of conversion function ( $f(\alpha)$ ) may be described in terms of the reaction-rate controlling Avrami-Erofeev (A-E) model (Avrami, 1939, 1940, 1941; Hardiman et al., 2005; Malecka et al., 2004). This kinetics was originally applied to model the phase transformations of steel. Later on, it found numerous applications in kinetics of crystallization, precipitation, decomposition of various solids, thin film growth and polymerization. Recently, this model has been successfully used to analyze the TPR and TPO reduction and oxidation data of both bulk and supported metal oxides (Richardson et al., 2004; Hardiman et al., 2005; Kanervo and Krause, 2001, 2002).

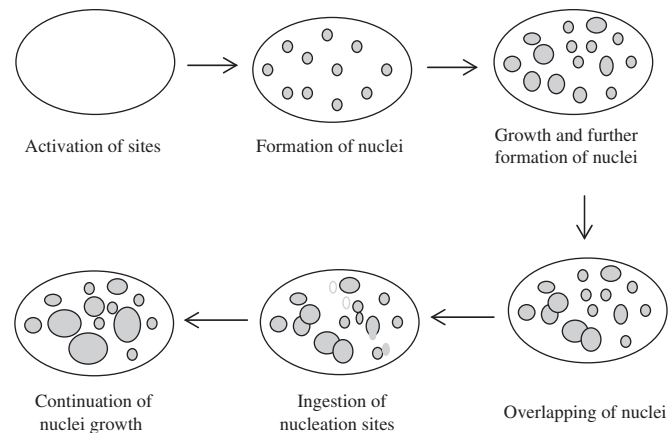


Fig. 5. Formation and growth of nuclei of product during the reduction/oxidation of oxygen carrier (Hossain and de Lasa, 2008).

According to the A-E model, the reduction and oxidation of the supported metal oxide proceeds through nucleation and a possible crystal growth with this leading to the following equation (Hossain and de Lasa, 2007; Brown, 2001; Kanervo and Krause, 2001):

$$f(\alpha) = n(1 - \alpha)[-\ln(1 - \alpha)]^{(n-1)/n} \quad (10)$$

where,  $n$  is the Avrami exponent indicative of the reaction mechanism and crystal growth dimension. Different values of the  $n$  parameter lead to various random nucleation, two-dimensional nuclei growth and three-dimensional nuclei growth.

Substituting Eqs. (9) and (10) in the fundamental kinetic equation Eq. (8) yields,

$$\frac{d\alpha}{dt} = nk_0 \exp \left[ \frac{-E_{app}}{R} \left( \frac{1}{T} - \frac{1}{T_m} \right) \right] \times (1 - \alpha)[-\ln(1 - \alpha)]^{(n-1)/n} \quad (11)$$

where  $E_{app}$  can be interpreted as the difference between the activation energy for growth and the activation energy for nucleation (Hossain and de Lasa, 2007).

**3.2.2.2. Unreacted shrinking-core model.** In general, the unreacted shrinking-core models are classified as (i) the grain model, which describe the solid reactant phase as a juxtaposition of dense objects and (ii) the pore model, which consider the porous solid as a collection of hollow objects (Patisson and Ablitzer, 2002). Apart from the mass transfer limitations, considering the surface reaction, the models are only different in terms of structural description (grain or pores), which essentially leads to differences in calculating the surface area of the active sites. In fact, the models of the above classification are not totally independent and each of these models can possibly be derived from a more generalized mathematical form depending upon the appropriate structure of the solid material.

Therefore, it was decided to consider a general texture model for reduction and oxidation of Co–Ni/Al<sub>2</sub>O<sub>3</sub>, with key model parameters being defined on the basis of physical characterization of the prepared oxygen carrier particles. As a result, the disappearance of the moles of solid reactant (oxygen) while the reduction process is progressing is given by

$$C_{NiO,0} W_{OC} \frac{d\alpha}{dt} = br_m \quad (12)$$

where,  $C_{NiO,0}$  is the initial molar concentration of NiO/Ni in the oxygen carrier,  $W_{OC}$  is the weight of the oxygen carrier,  $\alpha$  is the particle conversion,  $b$  is the stoichiometric coefficient of NiO and  $r_m$  is the

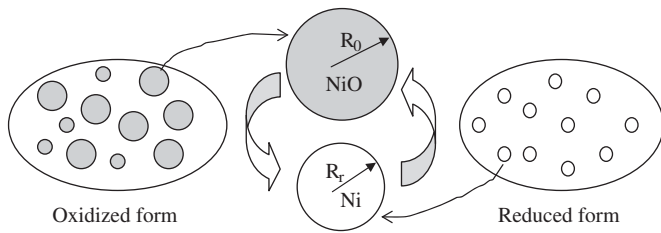


Fig. 6. Scheme of the shrinking-core reaction model (Hossain and de Lasa, 2008).

rate of reaction per unit mass of the oxygen carrier, assuming the density of the carrier particles is not changed significantly during reduction.

Since, the reaction is controlled by the chemical process, the reaction rate per unit mass in the balance equation can be directly related to the reaction per unit surface area of the solid particles, thus

$$r_m = a_0 S(\alpha) r_s \quad (13)$$

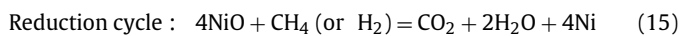
where,  $a_0$  is the initial specific surface area of oxygen carrier,  $r_s$  specific surface reaction rate and  $S(\alpha)$  reflects the change in the area of the reaction surface as a function of particle conversion. This function depends on the structure of the oxygen carrier particles.

Combining Eqs. (12) and (13) yields

$$\frac{d\alpha}{dt} = \frac{a_0 b}{C_{\text{NiO},0} W_{\text{OC}}} S(\alpha) r_s \quad (14)$$

In a gas–solid reaction both the crystal size of solid reactant and the porosity of the support material often provide important information about the reaction kinetics. For instance, the porosity of the solid carrier will change if the molar volumes of the reactant and product solid materials are different (Patisson and Ablitzer, 2002).

Considering the reduction and oxidation of the oxygen carrier particle and the stoichiometric ratio between the molar volume of NiO and Ni, the following can be advanced:



$$Z = \frac{4\nu_{\text{Ni}}}{4\nu_{\text{NiO}}} = \frac{4 \times 6.59}{4 \times 10.97} = 0.6 < 1 \quad (16)$$



$$Z = \frac{2\nu_{\text{NiO}}}{2\nu_{\text{Ni}}} = \frac{2 \times 10.97}{2 \times 6.59} = 1.7 > 1 \quad (18)$$

Therefore, after reduction the porosity of the carrier material will be increased due to the shrinkage of the particle volume inside the pores. It will be the opposite effect as well after re-oxidation of the oxygen carrier particle.

Fig. 6 illustrates the schematics of the cyclic reduction and oxidation process described by spherical shrinking-core model. According to the shrinking-core spherical grain model the particle conversion is obtained from the changing volume of the particle

$$\alpha = 1 - \frac{\text{volume of unreacted core}}{\text{volume of total particle}} = 1 - \left(\frac{r_{\text{OC}}}{R_{\text{OC}}}\right)^3 \quad (19)$$

therefore, the function  $S(\alpha)$  (in Eq. (14)) can be expressed as

$$a_0 S(\alpha) = 4\pi R_{\text{OC}}^2 (1 - \alpha)^{2/3} \quad (20)$$

Finally, the surface reaction rate ( $r_s$ ) can be derived assuming that the reaction between the gas-phase  $\text{H}_2$   $\text{CH}_4$  and solid NiO phase is the sole heterogeneous reaction taking place, since both XRD and TPR (Hossain and de Lasa, 2007) suggests negligible amount of aluminate reduction in the 550–650 °C temperature range.

Furthermore, earlier studies suggested that the alumina supported NiO reduction proceeds through adsorption of reducing gas ( $\text{H}_2/\text{CH}_4$  in this case) on the NiO and/or Ni sites as sites become available followed by rupture of Ni–O bonds to produce the metallic Ni,  $\text{CO}_2$  and  $\text{H}_2\text{O}$  (Richardson et al., 2004; Bandrowski et al., 1962). In such models both adsorption and desorption processes were considered faster steps than the surface reaction.

Thus, considering a first order reaction with respect to  $\text{H}_2/\text{CH}_4/\text{O}_2$  the surface reaction rate can be formulated as

$$r_s = k_s C_{\text{H}_2/\text{O}_2} = k_s (1 - \alpha) \quad (21)$$

where  $a$  is the stoichiometric ratio between the gas-phase and solid-phase conversions.

Substituting Eqs. (20) and (21) in Eq. (14) and substituting for Arrhenius equation (Eq. (9)) yields,

$$\frac{d\alpha}{dt} = k_0 \exp\left[\frac{-E}{R}\left(\frac{1}{T} - \frac{1}{T_m}\right)\right] (1 - \alpha)^{2/3} (1 - \alpha) \quad (22)$$

where

$$k_0 = \frac{a_0 b}{C_{\text{NiO},0} W_{\text{OC}}} k_{s0}$$

### 3.2.3. Parameters estimation and model discrimination

The kinetic models presented described in this study were evaluated using the TPR and TPO data. For kinetics analysis the rate of solid-state conversions of the oxygen carrier were unequivocally related to the rate of consumption of the gaseous reactant (hydrogen/oxygen) during the temperature programmed experiments.

In order to eliminate the effects of the heating rate on the parameter estimation the TPR and TPO experiments were carried out at several linear heating rates (5, 10, 15, 20 °C/min). The position of the conversion maxima was varied depending on the heating rate. The reduction rate maxima were occurred between 50% and 60% conversion levels, while the oxidation maxima was observed between 30% and 40% conversion levels. Both the TPR and TPO experiments were highly reproducible with reduction/oxidation maxima temperature within  $\pm 3$  °C.

The nucleation and nuclei growth and shrinking-core models (Eqs. (11) and (22), respectively) were evaluated by a least square fitting of the model parameters using TPR/TPO data implemented in MATLAB. Parameters were estimated in 0–0.95 conversion range. The discrimination between the models was based on the correlation coefficient ( $R^2$ ), lower residual SSQ and the smaller individual confidence intervals for the model parameters. Given the  $R^2$  values and spans of the parameters obtained, it was concluded that the A-E model better fitting was achieved using an  $n$  value of 1. A random nucleation model (“ $n$ ” value of 1) was selected given the close to constant crystallite size hypothesized, during repeated reduction and oxidation cycles, which is an indication of the very limited crystallite growth between cycles (Hossain et al., 2007). At higher values of  $n$ , for instance  $n = 2$ , the  $R^2$  values were 0.8 instead of 0.99 and the spans were increased from 5–10% to 20–30%. When compared between the random nucleation model and the shrinking-core model, still the random nucleation model is more favorable considering higher  $R^2$  value and lower SSQ value.

For the purpose of further model discrimination, both models were evaluated using TPR/TPO data at different heating rates (5, 10, 15, 20 °C/min). Table 1 lists the estimated activation energies and frequency factors as a function of heating rates. In the case of the nucleation model, the activation energies and the frequency factor remain close to constant levels, at the different heating rates. On the other hand, the activation energy and frequency factors with the shrinking-core model varied in a much wider range (approximately 22%). Thus, these results confirm the adequacy of the random nucleation model over the shrinking-core model.

**Table 1**  
Estimated model parameters for TPR and TPO cycles at different heating rates.

Heating rate	Shrinking-core model			Nucleation model		
	$E$ (kJ/mol)	$k_0 \times 10^4$	$\gamma^*$	$E$ (kJ/mol)	$k_0 \times 10^4$	$\gamma^*$
<i>Reduction</i>						
5 (°C/min)	69.12 ± 1.7	276 ± 5	0.54	45.9 ± 0.5	292 ± 1	0.55
10 (°C/min)	67.75 ± 1.22	556 ± 8	0.64	45.2 ± 1.1	378 ± 4	0.51
15 (°C/min)	72.2 ± 3	536 ± 2	0.50	46.84 ± 0.7	434 ± 4	0.45
20 (°C/min)	80.1 ± 4	400 ± 25	0.55	52.35 ± 2	394 ± 6.3	0.53
<i>Oxidation</i>						
5 (°C/min)	52.5 ± 5.3	445 ± 7	0.43	48.2 ± 3.1	387 ± 5	0.56
10 (°C/min)	68.6 ± 4.6	586 ± 10	0.47	43.7 ± 0.6	368 ± 2	0.40
15 (°C/min)	76.2 ± 5.6	533 ± 12	0.58	45.4 ± 3.5	352 ± 4	0.49

Note: Repeats displayed a typical ± 2.2% standard deviation;  $\gamma^*$ : cross-correlation coefficient.

Figs. 7a and b show the comparison between the experimental and nucleation model (for  $n = 1$ ) predicted conversions during both reduction and oxidation cycles of the oxygen carrier samples. One can notice that when data points are compared with model predictions there is a normal distribution of residuals with high correlation coefficients.

The activation energy for the reduction of the Co–Ni/Al<sub>2</sub>O<sub>3</sub> oxygen carrier varies between 45 and 110 kJ/mol, which is within the range (17–135 kJ/mol) reported by many researchers (Richardson et al., 2003). According to these studies, the activation energy falls into three groups depending on the reduction rate-controlling regime. A first group exhibiting low activation energy (15–25 kJ/mol) with external or very strong pore diffusional resistance limiting the overall reaction. A second group with activation energies of 40–50 kJ/mol with pore diffusion controlling the reduction reaction. Finally a third group, with activation energy in the 65–135 kJ/mol range displaying a chemically reaction controlled reduction.

One should notice that the reduction activation energy for various heating rates (Table 1) estimated by from the nucleation model, falls within the internal mass transfer controlled region. As already stated, activation energies in Eq. (15) represent a difference between activation energy for nucleation and crystal growth (Hossain and de Lasa, 2007). As a result, changes of measured activation energy may simply reflect nucleation and crystal growth energy of activation relative variations and one should be rather cautious with the phenomenological interpretation of these changes.

### 3.2.4. Model evaluation using CREC Riser Simulator data

The kinetics parameters of the prepared Co–Ni/Al<sub>2</sub>O<sub>3</sub> oxygen carrier were determined by using CREC fluidized Riser Simulator data. As mentioned in the experimental section, this reactor can be operated in batch reactor mode under turbulent fluidized bed reactor conditions. Therefore, it allows generating conversion data for different reaction times, which is essential to estimate the kinetics parameters in the differential equation (Eq. (11)) describing the reduction kinetics of the solid particles. Another important matter is the variation of the gas composition at various sections of the actual fluidized bed reactors. In fluidized bed CLC system the oxygen carrier is reduced by the gaseous fuel under different environments at different location of the fluidized bed reactors. At the bottom the of the fuel reactor the oxygen carrier particle will be in contact with only the pure fuel and along the length of the reactor the composition will be varied due to the formation of CO<sub>2</sub> and H<sub>2</sub>O by combustion reaction. Therefore, the kinetics investigation experiments should incorporate those effects for their appropriate representation in the kinetics models and the estimated parameters. Fortunately, the turbulent mixing in the CREC fluidized bed Riser Simulator also simulates the effects of the formed products at different contact times (de Lasa, 1992). For

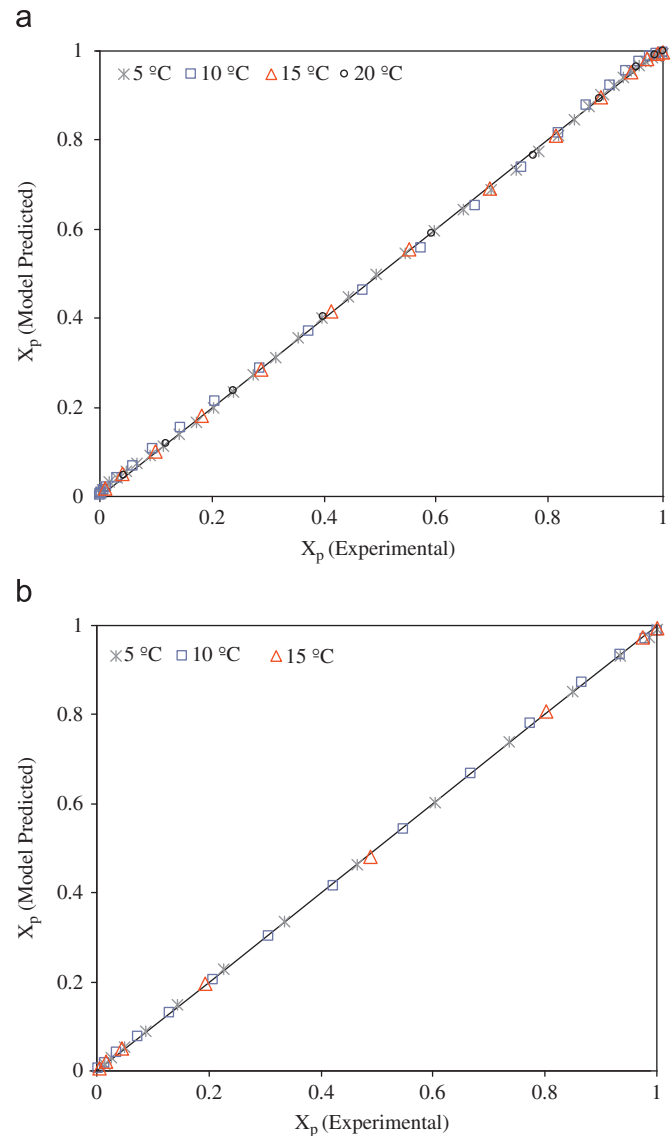


**Fig. 7.** Parity plots for non-isothermal conversions (reduction and oxidation) of Co–Ni/Al<sub>2</sub>O<sub>3</sub> oxygen carrier at different heating rates with nucleation and nuclei growth model: (a) TPR cycle (b) TPO cycle (Note: Reported points are one every 2 minutes to avoid the figure to be overcrowded. The original data file includes data points taken every two seconds).

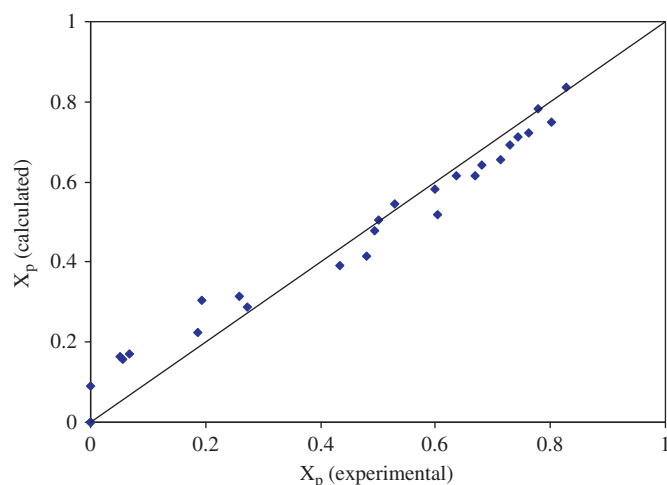


**Fig. 8.** Parity plot for conversion of oxygen carrier during fuel combustion cycle in the CREC Riser Simulator using  $\text{CH}_4$  as fuel with nucleation and nuclei growth model ( $n = 1$ ) ( $T$ : 550–650 °C;  $P$ : 1 atm;  $W_{\text{carrier}}$ : 50 mg;  $V_{\text{CH}_4}$  inj.: 10 mL).

**Table 2**

Comparison of estimated parameters for the reduction of Co–Ni/Al<sub>2</sub>O<sub>3</sub> oxygen carrier using TPR and CREC Riser Simulator data.

Sample ID	Fuel	$E$ (kJ/mol)	$k_0$	$R^2$	$\gamma^*$
TPR data	H <sub>2</sub>	45.1 ± 1	(260 ± 4) × 10 <sup>-4</sup>	0.99	0.51
CREC Riser Simulator data	CH <sub>4</sub>	49.0 ± 1	(34.1 ± 28.4) × 10 <sup>-4</sup>	0.97	0.63

$\gamma^*$ : cross-correlation coefficient.

further confirmation, several preliminary experiments were carried with different mixed feed ( $\text{CH}_4$  and  $\text{CO}_2$ ) compositions and found that the product  $\text{CO}_2$  has no effect on the conversion of the oxygen carrier at studied reaction conditions. Garcia-Labiano et al. (2006) also reported the absence of product effects on the conversion of NiO and CuO based oxygen carriers. Consequently, the following experiments were carried out using pure  $\text{CH}_4$  as feed. To determine the kinetics parameters the experiments were conducted at three different temperature levels (550, 600 and 650 °C) and at close to constant atmospheric pressure (1.2 atm). For each temperature level isothermal conversion data were collected for various reaction times.

The estimated activation energy and pre-exponential factors with their 95% confidence limits are  $49 \pm 10$  (kJ/mol) and  $(34.1 \pm 28.4) \times 10^{-3}$ , respectively. The corresponding correlation coefficient for the estimated values is 0.97. Finally, the values of the established kinetic parameters were introduced into the nucleation and nuclei growth model (Eq. (11)) and the differential equation was solved to predict the particle conversion for different reaction time. Fig. 8 compares the experimental and model predicted particle conversion during the reduction reaction at different temperature levels. It is interesting to see that the nucleation and nuclei growth model with  $n = 1$  fits the experimental data adequately.

Table 2 provides a comparison of the estimated energy of activation for the reduction of Co–Ni/Al<sub>2</sub>O<sub>3</sub> oxygen carrier using TPR and the CREC Riser Simulator. It is encouraging to see the consistency of the energy of activation obtained using these two different experimental set-ups. This activation energies for Co–Ni/Al<sub>2</sub>O<sub>3</sub> reduction is found to be in the lower than the 54 kJ/mol activation energies for the unprompted Ni/Al<sub>2</sub>O<sub>3</sub> reduction (Hossain and de Lasa, 2007) with this confirming the favorable effect of Co on the reducibility of the bimetallic oxygen carrier.

## 4. Conclusions

Physicochemical characterization and kinetic study of Co–Ni/Al<sub>2</sub>O<sub>3</sub> oxygen carrier sample reveal the following:

- XRD of Co doped fresh Co–Ni/Al<sub>2</sub>O<sub>3</sub> oxygen carrier sample indicates that mainly NiO/Ni is the reducible/oxidizable phase of the oxygen carrier.
- Pulse chemisorption demonstrates that Co–Ni/Al<sub>2</sub>O<sub>3</sub> sample shows consistent metal dispersion/re-dispersion over the repeated reduction/oxidation cycles.
- The nucleation and nuclei growth model with random nucleation mechanism ( $n = 1$ ) is found to describe the experimental data adequately, with various parameters being determined with their appropriate statistical spans for good fitting.
- The activation energies for Co–Ni/Al<sub>2</sub>O<sub>3</sub> reduction is found to be in the 45 kJ/mol level significantly lower than the 54 kJ/mol activation energies for the unprompted Ni/Al<sub>2</sub>O<sub>3</sub> reduction. This confirms the favorable effect of Co on the reducibility of the bimetallic oxygen carrier.

## Notation

$a_0$	initial specific surface area of oxygen carrier, m <sup>2</sup> /g
$b$	stoichiometric coefficient of the solid phase reactant
$C_{\text{NiO},0}$	initial molar concentration of NiO/Ni in the oxygen carrier, mol/g carrier
$d_p$	particle diameter, cm
$d_{\text{pore}}$	pore diameter, nm
$d_{\text{XRD}}$	the volume average diameter of the crystallite, nm
$E_{\text{app}}$	apparent activation energy for oxidation/reduction, kJ/mol
$k$	specific rate of the overall reaction, mol/s
$K_s$	shape factor of the growing particles
$n$	dimensions of the growing crystals
$p_i$	partial pressure of the gas phase reactant $i$ , kPa
$P_a$	pressure, kPa
$r_m$	rate of reaction per unit mass of the oxygen carrier
$r_s$	specific surface reaction rate
$R_p$	particle radius, cm
$S$	surface area as a function of particle conversion (m <sup>2</sup> /g)
$T_m$	centering temperature, K
$W_{\text{OC}}$	weight of the oxygen carrier, g
$X_{\text{CH}_4}$	conversion of methane

## Greek letters

$\alpha$	degree of conversion of oxygen carrier
$\alpha_{\text{total}}$	extended degree of conversion of the oxygen carrier
$\beta$	rate of temperature increase, K/min
$\theta$	contact angle
$\lambda$	radiation wave length (Å)
$\rho_p$	particle density, g/cc
$\sigma$	surface tension, N/m <sup>2</sup>

## Acknowledgments

M.M.H. wishes to acknowledge the Natural Sciences and Engineering Research Council of Canada (NSERC) for Canada Graduate Scholarship for Doctoral study (CGS-D) and The University of Western Ontario for President's Scholarship for Graduate Study (PSGS). The authors also like to thank NSERC for their financial support to this project.

## References

- Abad, A., Adanez, J., Gracia-Labiano, F., de Diego, L.F., Gayan, P., Celaya, J., 2007. Mapping of the range of operational conditions for Cu-, Fe-, and Ni-based oxygen carriers in chemical-looping combustion. *Chemical Engineering Science* 62, 533–549.
- Adanez, J., de Diego, L.F., Garcia-Labiano, F., Gayan, P., Abad, A., 2004. Selection of oxygen carriers for chemical-looping combustion. *Energy & Fuels* 18, 371–377.
- Avrami, M., 1939. Kinetics of phase change. I. *Journal of Chemical Physics* 7, 1103–1112.
- Avrami, M., 1940. Kinetics of phase change. II. *Journal of Chemical Physics* 8, 212–224.
- Avrami, M., 1941. Kinetics of phase change. III. *Journal of Chemical Physics* 9, 177–184.
- Bandrowski, J., Bickling, C.R., Yang, K.H., Hougen, O.A., 1962. Kinetics of nickel oxide by hydrogen. *Chemical Engineering Science* 17, 379–390.
- Bolt, P.H., Habraken, F.H.P.M., Geus, J.W., 1998. Formation of nickel, cobalt, copper, and iron aluminates from  $\alpha$ - and  $\gamma$ -alumina-supported oxides: a comparative study. *Journal of Solid State Chemistry* 135, 59–69.
- Brown, M.E., 2001. *Introduction to Thermal Analysis: Techniques and Applications*, second ed. Kluwer Academic Publishers, Dordrecht, The Netherlands. pp. 181–210.
- de Lasa, H.I., 1992. Riser simulator for catalytic cracking studies. US Patent 5, 102, 628.
- Fogler, H.S., 1999. *Element of Chemical Reaction Engineering*, third ed. Prentice Hall Int. Inc., Englewood Cliffs, NJ. pp. 758–759.
- Garcia-Labiano, F., Adanez, J., de Diego, L.F., Gayan, P., Abad, A., 2006. Effect of pressure on the behavior of copper-, iron-, and nickel-based oxygen carrier for chemical-looping combustion. *Energy & Fuel* 20, 26–33.
- Gavalas, G.R., Phichitkul, C., Voecks, G.E., 1984. Structure and activity of NiO/ $\alpha$ -Al<sub>2</sub>O<sub>3</sub> and NiO/ZrO<sub>2</sub> calcined at high temperatures. I. Structure. *Journal of Catalysis* 88, 54–64.
- Hardiman, K.M., Cooper, C.G., Adesina, A.A., 2004. Multiple analysis of the role of preparation conditions on the intrinsic properties of Co-Ni/Al<sub>2</sub>O<sub>3</sub> steam-reforming catalyst. *Industrial and Engineering Chemistry Research* 43, 6006–6013.
- Hardiman, K.M., Hsu, C.H., Ying, T.T., Adesina, A.A., 2005. The influence of impregnating pH on the postnatal and steam reforming characteristics of a Co-Ni/Al<sub>2</sub>O<sub>3</sub> catalyst. *Journal of Molecular Catalysis A: Chemical* 239, 41–48.
- Heynderickx, G.J., Schools, E.M., Marin, G.B., 2005. Coke combustion and gasification kinetics in ethane steam crackers. *AI.Ch.E. Journal* 51 (5), 1415–1428.
- Hossain, M.M., 2007. Fluidized bed chemical-looping combustion: development of a bimetallic oxygen carrier and kinetic modeling. Ph.D. Dissertation, The University of Western Ontario, London, Ontario, Canada.
- Hossain, M.M., de Lasa, H.I., 2007. Reactivity and stability of Co-Ni/Al<sub>2</sub>O<sub>3</sub> oxygen carrier in multicycle CLC. *AI.Ch.E. Journal* 53, 1817–1829.
- Hossain, M.M., de Lasa, H.I., 2008. Chemical-looping combustion (CLC) for inherent CO<sub>2</sub> separation—a review. *Chemical Engineering Science* 63, 4433–4451.
- Hossain, M.M., Sedor, K.E., de Lasa, H.I., 2007. Co-Ni/Al<sub>2</sub>O<sub>3</sub> oxygen carrier for fluidized bed chemical-looping combustion: desorption kinetics and metal-support interaction. *Chemical Engineering Science* 62, 5464–5472.
- Ishida, M., Jin, H., 1996. A novel chemical-looping combustor without NO<sub>x</sub> formation. *Industrial & Engineering Chemistry Research* 35, 2469–2472.
- Jin, H., Okamoto, T., Ishida, M., 1999. Development of novel chemical-looping combustion: synthesis of solid looping material of Ni/NiAl<sub>2</sub>O<sub>4</sub>. *Industrial & Engineering Chemistry Research* 38, 126–132.
- Kanervo, J.M., Krause, A.O.I., 2002. Characterization of supported chromium oxide catalysts by kinetics analysis of H<sub>2</sub>-TPR data. *Journal of Catalysis* 207, 57–65.
- Kanervo, J.M., Krause, A.O.I., 2001. Kinetics analysis of temperature-programmed reduction: behavior of a CrO<sub>x</sub>/Al<sub>2</sub>O<sub>3</sub> catalyst. *Journal of Physical Chemistry B* 105, 9778–9784.
- Khodakov, A.Y., Bechara, R., Griboval-Constant, A., 2003. Fischer-Tropsch synthesis over silica supported cobalt catalysts: mesoporous structure versus cobalt surface density. *Applied Catalysis A: General* 254, 273–288.
- Khodakov, A.Y., Griboval-Constant, A., Bechara, R., Zholobenko, V.L., 2002. Pore size effects in Fischer Tropsch synthesis over cobalt-supported mesoporous silicas. *Journal of Catalysis* 206, 230–241.
- Koga, Y., Harrison, L.G., 1984. In: Bamford, C.H., Tipper, C.F.H., Compton, R.G. (Eds.), *Comprehensive Chemical Kinetics*, vol. 21. Elsevier, Amsterdam, p. 120.
- Lemaitre, J.L., Menon, P.G., Delannay, F., 1984. The measurement of catalyst dispersion. In: Delannay, F. (Ed.), *Characterization of Heterogeneous Catalysts*, vol. 15. Dekker, New York.
- Levenspiel, O., 1999. *Chemical Reaction Engineering*, third ed. Wiley, New York. pp. 566–586.
- Malecka, B., Crodz-Ciesla, E., Malecki, A., 2004. Mechanism and kinetics of thermal decomposition of zinc oxalate. *Thermochemica Acta* 423, 13–18.
- Patisson, F., Ablitzer, D., 2002. Physicochemical and thermal modeling of the reaction between a porous pellet and a gas. *Power Technology* 128, 300–305.
- Richardson, J.T., Lei, M., Turk, B., Forster, K., Twigg, M.V., 1994. Reduction of model steam reforming catalysts: NiO/ $\alpha$ -Al<sub>2</sub>O<sub>3</sub>. *Applied Catalysis A: General* 110, 217–237.
- Richardson, J.T., Scates, R.M., Twigg, M.V., 2003. X-ray diffraction of nickel oxide reduction by hydrogen. *Applied Catalysis A: General* 246, 137–150.
- Richardson, J.T., Scates, R.M., Twigg, M.V., 2004. X-ray diffraction of hydrogen reduction of NiO/ $\alpha$ -Al<sub>2</sub>O<sub>3</sub> steam reforming catalysts. *Applied Catalysis A: General* 267, 35–46.
- Richardson, J.T., Turk, B., Twigg, M.V., 1996. Reduction of model steam reforming catalysts: effect of oxide additives. *Applied Catalysis A: General* 148, 97–112.
- Ryu, H.-J., Bae, D.-H., Han, K.-H., Lee, S.-Y., Jin, G.-T., Choi, J.-H., 2001. Oxidation and reduction characteristics of oxygen carrier particles and reaction kinetics by unreacted core model. *Korean Journal of Chemical Engineering* 18, 831–837.
- Sedor, K.E., Hossain, M.M., de Lasa, H.I., 2008a. Reactivity and stability of Ni/Al<sub>2</sub>O<sub>3</sub> oxygen carrier for chemical-looping combustion (CLC). *Chemical Engineering Science* 63 (11), 2994–3007.
- Sedor, K.E., Hossain, M.M., de Lasa, H.I., 2008b. Reduction kinetics of a fluidizable nickel-alumina oxygen carrier for chemical-looping combustion. *Canadian Journal of Chemical Engineering* 86, 323–334.
- Sohn, H.Y., Szekeley, J., 1972. A structural model for gas–solid reaction with moving boundary-III. A general dimensionless representation of the irreversible reaction between a porous solid and reactant gas. *Chemical Engineering Science* 27, 763–778.
- Szekeley, J., Lin, C.I., Sohn, H.Y., 1973. A structural model for gas–solid reaction with moving boundary-V. An experimental study of the reduction porous nickel-oxide pellets with hydrogen. *Chemical Engineering Science* 28, 1975–1989.
- Takanabe, K., Ngaoka, K., Nariai, K., Aika, K., 2005. Titani-supported cobalt and nickel bimetallic catalysts for carbon dioxide reforming of methane. *Journal of Catalysis* 232, 268–275.
- Utigard, T.A., Wu, M., Plascencia, G., Marin, T., 2005. Reduction kinetics of Goro nickel oxide using hydrogen. *Chemical Engineering Science* 60, 2061–2068.